Nanostructures and thin films of transparent conductive oxides studied by perturbed angular correlations

M. B. Barbosa (IFIMUP-IN, Porto U.), J. N. Gonçalves (CICECO, Aveiro U.), A. Redondo-Cubero (CFNUL, ITN, Sacavem), S. M. C. Miranda (ITN, Sacavem), R. Simon (Bonn U., HISKP), P. Kessler (Bonn U., HISKP), M. Brandt (Humboldt-U., Berlin), F. Henneberger (Humboldt-U., Berlin), E. Nogales (U. Complutense, Madrid), B. Méndez (U. Complutense, Madrid), K. Johnston (Saarland U.), E. Alves (CFNUL, ITN, Sacavem), R. Vianden (Bonn U., HISKP), J. P. Araújo (IFIMUP-IN, Porto U.), K. Lorenz (ITN, Sacavem), J. G. Correia (ITN, Sacavem)

Published in: Phys. Status Solidi B 250, No. 4, 801-808 (2013)

DOI: 10.1002/pssb.201200923

The final publication is available at
http://onlinelibrary.wiley.com/doi/10.1002/pssb.201200923/abstract

Nanostructures and thin films of transparent conductive oxides studied by perturbed angular correlations

M. B. Barbosa[*,1], J. N. Gonçalves[2], A. Redondo-Cubero[3,4], S. M. C. Miranda[3], R. Simon[5], P. Kessler[5], M. Brandt[6], F. Henneberger[6], E. Nogales[7], B. Méndez[7], K. Johnston[8], E. Alves[3,4], R. Vianden[5], J. P. Araújo[1], K. Lorenz[3,4], J. G. Correia[3,4]

[1] IFIMUP and IN-Institute of Nanoscience and Nanotechnology, Departamento de Física e Astronomia da Faculdade de Ciências da Universidade do Porto, Rua do Campo Alegre, 687, 4169-007 Porto, Portugal
[2] Departamento de Física and CICECO, Universidade de Aveiro, Campus Universitário de Santiago, P-3810-193 Aveiro, Portugal
[3] IST/ITN, Instituto Superior Técnico, Universidade Técnica de Lisboa, Estrada Nacional 10, 2686-953, Sacavém, Portugal
[4] Centro de Física Nuclear da Universidade de Lisboa, Avenida Professor Gama Pinto 2, 1649-003 Lisboa, Portugal
[5] Helmholtz-Institut für Strahlen- und Kernphysik, Universität Bonn, 53115 Bonn, Germany
[6] Institut für Physik, Humboldt-Universität zu Berlin, Newtonstr. 15, 12489 Berlin, Germany
[7] Departamento de Física de Materiales, Facultad de Ciencias Físicas, Universidad Complutense, E-28040 Madrid, Spain
[8] Technische Physik, Universität des Saarlandes, 66041 Saarbrücken, Germany

Received XXXX, revised XXXX, accepted XXXX
Published online XXXX

Key words: PAC, ion implantation, lattice location, ZnO, $CdZnO$, Ga_2O_3, DFT

[*] Corresponding author: e-mail marcelo.barbosa@fc.up.pt, Phone: (+351) 22 04 02 362 , Fax: (+351) 22 04 02 406

The versatility of perturbed angular correlations (PAC) in the study of nanostructures and thin films is demonstrated, namely for the specific cases of $ZnO/Cd_xZn_{1-x}O$ thin films and Ga_2O_3 powder pellets and nanowires, examples of transparent conductive oxides. PAC measurements as a function of annealing temperature were performed after implantation of $^{111m}Cd/^{111}Cd$ ($T_{1/2} = 48\,min.$) and later compared to density functional theory simulations.

For ZnO, the substitution of Cd probes at Zn sites was observed, as well as the formation of a probe-defect complex. The ternary $Cd_xZn_{1-x}O$ ($x = 0.16$) showed good macroscopic crystal quality but revealed some clustering of local defects around the probe Cd atoms, which could not be annealed. In the Ga_2O_3 samples, the substitution of the Cd probes in the octahedral Ga-site was observed, demonstrating the potential of ion-implantation for the doping of nanowires.

1 Introduction In the past decades, the development of integrated circuits has been responsible for a true revolution in electronics and photonics applications. However, with increasing miniaturization following Moore's law and the integration of nanotechnology in device applications, new and unpredicted properties are revealed, with potential applications to industry. Moreover, the modelling of these properties faces the fact that the smaller the devices get, the more they depend on the scale factor, geometry, symmetry and localized interactions of defects and impurities that can no longer be considered diluted and treated like "perturbations". Therefore, in this highly integrated new world the small scale rules both new properties and new problems. The future of potentially relevant nano-materials relies on both tunable properties and on large-scale integration feasibility [1].

Nanostructures and thin film technologies might merge together where ion implantation is still envisaged as an integrated part of the processes. Still, ion implantation carries along with the benefits - universal dopant and profile

tuning - intrinsic nuisances, i.e., defect generation. Willing to contribute to the better understanding of doping and processing by ion beams, we present here two examples of studies performed with the nanoscopic Perturbed Angular Correlation technique (PAC). PAC probes the charge density distribution in the surroundings of chosen radioactive nuclei, thus allowing characterizing the probe's real environment at the atomic scale. We have chosen to study ZnO and $Cd_xZn_{1-x}O$ thin films - aimed to cover luminescence wavelengths from UV to yellow [2] - and the technologically relevant high -K factor Ga_2O_3 nanostructures and Ga_2O_3 pellets [3]. Both materials belong to the family of transparent conductive oxides and the used PAC probe, $^{111m}Cd/^{111}Cd$, is well suited to study the microscopic physical properties of these materials being an isoelectronic impurity in the case of ZnO and a possible p-type dopant in the case of Ga_2O_3.
For each case, we show how and to which extent the local environment of the implanted Cd is reconstructed to the one of the host crystalline matrix as a function of annealing temperature. We further attempt to identify local defects and the probes lattice site by comparing the experimental results with first principle simulations.

1.1 About the PAC technique PAC has been widely used in solid state physics to study the local atomic environment of radioactive probe atoms since it accurately measures the electric field gradient (EFG) at a probe's site, which is highly sensitive to the charge density distribution surrounding the nuclei [4]. In this method, a radioactive probe is introduced into the sample and the time dependence of the angular correlation between two emitted photons in a γ-γ cascade decay is measured, with the first γ starting the measurement and the second γ stopping it. The hyperfine interaction of the EFG at the probe site with the electric quadrupole moment Q of the intermediate state of the cascade causes a time dependent perturbation in the emission direction of the second γ with respect to the emission direction of the first γ. The time dependent oscillations in the anisotropic emission of the second γ define the observable frequency ω_0 which is proportional to the quadrupole interaction frequency ω_Q

$$\omega_0 = k\,\omega_Q,\ \omega_Q = \frac{eQV_{zz}}{4I(2I-1)\hbar} \qquad (1)$$

where I is the spin and Q is the electric quadrupole moment of the intermediate state, V_{zz} is the principal component of the EFG and k is equal to 3(6) for integer(half-integer) spin. Since the EFG is a traceless matrix, it can be completely described by the V_{zz} component and the axial asymmetry parameter η defined as $\eta = (V_{xx} - V_{yy})/V_{zz}$ [4]. The existence of lattice imperfections or impurities causes different EFGs in the probe's environment and thus a distribution of frequencies around a central value that induces an attenuation of the angular correlation. The distribution function, usually approximated by a Lorentzian, is then defined by the central frequency ω_0 and the full width at half maximum $FWHM$.

1.2 Case studies: $ZnO/Cd_xZn_{1-x}O$ & Ga_2O_3 Zinc Oxide is subject of intense research due to its remarkable properties for optoelectronics, mainly for devices in the blue and UV range [5]. Its wide band-gap ($3.37\,eV$ at room temperature) makes it desirable to adjust its electrical, optical and magnetic properties through doping with selective elements [6]. Futhermore, the possibility of growing pseudobinary compounds with MgO and CdO allows bandgap tuning and heterostructure growth. In particular, ternary $Cd_xZn_{1-x}O$ alloys allow band-gap engineering in a wide range that covers the UV-yellow spectral region [2]. However, ZnO and CdO have different crystalline structures, wurtzite and rock salt, respectively, being difficult to stabilize a wurtzite phase of $Cd_xZn_{1-x}O$, which frequently results in phase separation [7,8]. The solubility of CdO in ZnO, besides being low, depends strongly on the growth conditions and technique that is used. Concerning PAC studies, ZnO bulk crystals have been studied using different probes [9] but, for technological purposes, thin films must be used. Thus, in this study, thin films of ZnO and $Cd_xZn_{1-x}O$ ($x = 0.16$) were investigated.
Gallium oxide (Ga_2O_3) has the biggest band-gap among the transparent conductive oxides, $4.8\,eV$, making it interesting for photonics working in the UV and visible wavelength region[3,10–13]. However, as in the case of ZnO, it is an intrinsic n-type semiconductor and it has been proven very difficult to obtain p-type doping, which is fundamental for technological applications. Nonetheless, its nanowires could be used as effective waveguides and optical doping using rare earth ions in-situ or by ion implantation has been demonstrated [3,13]. In this work we study the viability of ion implantation to incorporate dopants into these nanowires.

2 Technical details The ZnO thin film ($500\,nm$ thick) was grown by molecular beam epitaxy (MBE) on an a-plane sapphire substrate at $T_s = 380^oC$ and subsequently annealed at $T_A = 650^oC$ for 5 minutes. The $Cd_{0.16}Zn_{0.84}O$ thin film ($200\,nm$ thick) was grown at $T_s = 130^oC$ and annealed at $T_A = 400^oC$ for 4 hours. The film was grown on a $500\,nm$ thick $MgZnO$ buffer layer at $T_s = 380^oC$ on a-plane sapphire, the former serves to reduce the lattice mismatch and prevent the propagation of defects from the sapphire to the $Cd_{0.16}Zn_{0.84}O$ layer [2]. The structural characterization of these samples has been reported previously [14]. Two different samples of β-Ga_2O_3 were used, a powder pellet and nanowires (both polycrystalline-like, consisting of a distribution of randomly oriented micro-crystals, from the point of view of the PAC measurement). The nanowires were grown from metallic gallium in a tube furnace using a vapour-solid growth mechanism reported elsewhere [3]. The grain size of the pellet was in the range of several microns whereas the nanowires' length and thickness was up to tens of

microns and between tens to hundreds of nanometers, respectively.

Implantations were performed at ISOLDE/CERN with a $30\,keV$ energy beam of radioactive $^{111m}Cd/^{111}Cd$ ($T_{1/2} = 48\,min.$) to low fluences of $\sim 5 \times 10^{11}\ at/cm^2$, at room temperature (RT). γ-γ PAC experiments were done onto decay of ^{111m}Cd ($\gamma_1 = 150\,keV$, $\gamma_2 = 245\,keV$) to ^{111}Cd [15], whose intermediate state has an electric quadrupole moment of $Q = 0.83(13)\,b$ and spin $I = 5/2$ [16]. A BaF_2 6-detector PAC setup was used [17], but when measuring single crystals only one 4-detector plane of this setup was selected, where the sample's c-axis was oriented within the detector plane at 45^o with two 90^o detectors ($M45$ setup). In the case of $Cd_{0.16}Zn_{0.84}O$, a complementary orientation was measured with the c-axis perpendicular to the 4-detector plane ($M90$ setup). The samples were annealed under air atmosphere during 10 minutes in a conventional tube furnace and the measurements were performed at $T_M = RT$.

X-ray diffraction (XRD) was used to determine the lattice parameters of the ZnO and $Cd_{0.16}Zn_{0.84}O$ thin films yielding $a = 3.2405$ Å and $c = 5.2152$ Å for the ZnO and $a = 3.283$ Å and $c = 5.303$ Å for the $Cd_{0.16}Zn_{0.84}O$. The lattice parameters of the Ga_2O_3 powder samples and nanowires were previously found to be "relaxed" [18], i.e., with standard bulk parameters, thus the values $a = 12.23$ Å, $b = 3.08$ Å, $c = 5.80$ Å and $\beta = 107.3^o$, reported in ref.[10], were considered, which are in agreement with the optimum estimated atomic positions and lattice parameters found in the theoretical study of Ga_2O_3 done by F. Litimein *et al.* [19].

Additional characterization of the as-grown and as-implanted (and annealed) samples was carried out by Rutherford Backscattering Spectrometry in the channelling mode (RBS/C) using a $2\,MeV\ He^+$ beam with $4\,nA$ of current and a PIN diode detector at a backscattering angle of 165^o.

To simulate the EFG at the probe's site, a $3 \times 3 \times 2$ supercell of the wurtzite crystalline structure of ZnO was considered (72 atoms) with a ^{111}Cd probe located at one of the equivalent Zn sites, using first the lattice parameters measured by XRD on the film and second the lattice parameters of bulk ZnO, $a = 3.2489$ Å and $c = 5.2053$ Å, reported on ref.[20]. In the case of Ga_2O_3, a $1 \times 2 \times 2$ supercell of the β-Ga_2O3 crystalline structure was considered (80 atoms), using the lattice parameters reported in ref.[10]. Since the Ga atoms have two non-equivalent sites, octahedral and tetrahedral, two simulations were performed, considering the ^{111}Cd probe in each site. The simulations were performed *via* the L/APW+lo implementation of density functional theory (DFT), using the WIEN2k code [21]. The GGA-PBE exchange-correlation functionals and a cut-off value for the plane wave expansion of $R_{mt}K_{max} = 7.0$ were considered, where R_{mt} is the muffin-tin sphere radius and K_{max} is the largest K-vector of the plane wave expansion of the wave function. For

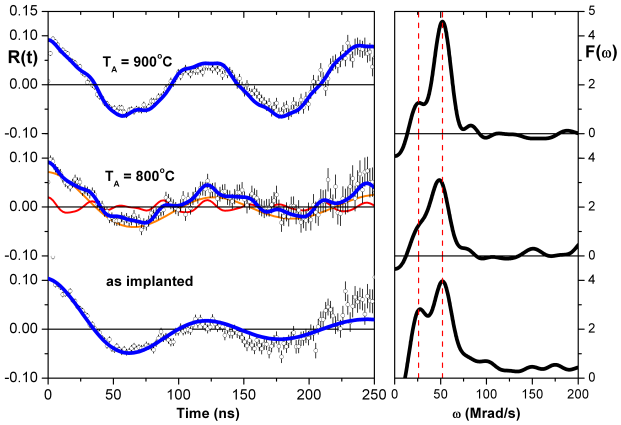

Figure 1 ^{111}Cd:ZnO γ-γ PAC from decay of ^{111m}Cd. Study as a function of annealing temperature under air. $T_M = RT$, Geometry: $M45$. **(left)** Counting rate ratio, $R(t)$. For $T_A = 800^oC$, besides $R(t)$, fraction 1 is represented in orange and fraction 2 in red, **(right)** Frequencies extracted from $R(t)$ after Fourier analysis.

ZnO, 24 k-points in the irreducible Brillouin zone were used, and 15 in the case of Ga_2O_3. The convergence of the calculations was examined with respect to $R_{mt}K_{max}$ and to the number of k-points until the chosen values resulted in a convergence of the total energy of the crystal of less than $1\,mRy$. Relaxation of the atomic positions was done in a self-consistent way by minimizing the atomic forces to a maximum limit of $1\,mRy/bohr$. Smaller super-cells were attempted but the actual sizes were found to be the minimum required for achieving proper dilution of ^{111}Cd at the DFT simulations.

3 Results and discussion

3.1 ZnO Figure 1 shows (left) the PAC experimental functions, the fits and (right) the corresponding cosine Fourier transform components from *ZnO* after implantation and as a function of the annealing temperature up to 900^oC. The obtained fitting parameters are presented in Table 1. The data clearly shows the existence of a main position/situation for the probes revealed by one EFG_1 distribution that is characterized by the central frequency $\omega_{01} \approx 26\,Mrad/s$ and $\eta = 0$. In the plot of the Fourier transform there are two dashed lines, corresponding to the observables $\omega_0 = 26\,Mrad/s$ and $2\omega_0 = 52\,Mrad/s$, to mark the two main frequency components of EFG_1 for all measurements, as expected for a probe with spin $5/2$ and V_{zz} collinear with the sample's c-axis. The existence of implantation defects is revealed by the important static distribution observed in the "as-implanted" sample that attenuates the frequency pattern at the $R(t)$ experimental function. In the absence of a second well-defined EFG signature, we conclude that most of these implantation defects are not correlated with the probe nuclei but

Table 1 ^{111}Cd:ZnO fitting parameters, related to Fig.1. ω_0 and $FWHM$ are given in $Mrad/s$ and V_{zz} is given in $10^{21}\,V/m^2$.

Annealing	Fraction 1					Fraction 2				
	Perc.	ω_0	V_{zz}	η	$FWHM$	Perc.	ω_0	V_{zz}	η	$FWHM$
900^oC	88%	26(-)	1.37(5)	0.0(-)	0.0(-)	12%	108(5)	5.7(1)	0.8(2)	0.0(-)
800^oC	78%	26(2)			4.5(7)	22%	111(1)	5.86(6)	0.6(3)	2.4(8)
As implanted	100%	26(1)			7.2(4)	-				

are randomly dispersed in the sample within the implantation and defect profiles. Upon increasing the annealing temperature to 800^oC, in addition to the first fraction of probe nuclei with observable frequency ω_{01}, a second fraction starts to be observed indicating that defects are now present in more localized sites. On the one hand the width of the static distribution of the main fraction is reduced indicating a greater dilution of uncorrelated defects. On the other hand, some of the defects could come closer to the probes and eventually be trapped by the impurity Cd atom to originate EFG_2, for a certain fraction of probe atoms. The results are in good agreement with previous works in ZnO implanted with ^{111}In and measured at the same ^{111}Cd state [22–24], where M. E. Mercurio *et al.* [22] obtained a main fraction with $\omega_{01} = 29.9(1)\,Mrad/s$ and a second fraction with $\omega_{02} = 142(5)\,Mrad/s$ in ZnO powders, assigning the last to interstitial sites or vacancy-related sites. H. Wolf *et al.* [23] obtained a main fraction with $\omega_{01} = 29.4(1)\,Mrad/s$ and a second fraction with $\omega_{02} = 174(1)\,Mrad/s$ in ZnO single crystals, assigning the last to trapped oxygen-vacancies. P. Kessler [24] confirmed the assigning of the larger frequency EFG to next-neighbour oxygen vacancies, based on the fact that PAC measurements performed in several different orientations gave similar results, which can be justified by the existence of 4 (almost) equivalent positions for oxygen near the Zn atoms. In our case, due to the small fraction for EFG_2, we have not implemented a multi-EFG orientation fitting regarding this fraction. After annealing at 900^oC the fraction of probes experiencing EFG_2 is decreasing suggesting that the probe-defect complex starts to dissociate at this temperature.

The smaller EFG_1 obtained for the thin film, compared to the one reported for bulk ZnO, can be explained by biaxial strain present in the epitaxial film. This assumption is confirmed by the DFT calculations, where the simulations carried out using the measured lattice parameters of the thin film resulted in a $V_{zz} = 1.374 \times 10^{21}\,V/m^2$ for the Cd probe in the Zn site, which is in perfect agreement with $V_{zz} = 1.37(5) \times 10^{21}\,V/m^2$ corresponding to the experimental frequency $\omega_{01} \approx 26\,Mrad/s$. Simulations using a variety of lattice parameters attributed for bulk ZnO were done in order to compare with the experimental results obtained by M. E. Mercurio *et al.* [22] ($V_{zz} = 1.58(2) \times 10^{21}\,V/m^2$ corresponding to the frequency $\omega_0 = 29.9(1)\,Mrad/s$) and by H. Wolf *et al.* [23] ($V_{zz} = 1.55(2) \times 10^{21}\,V/m^2$ corresponding to the frequency $\omega_{01} = 29.4(1)\,Mrad/s$). However, the lattice

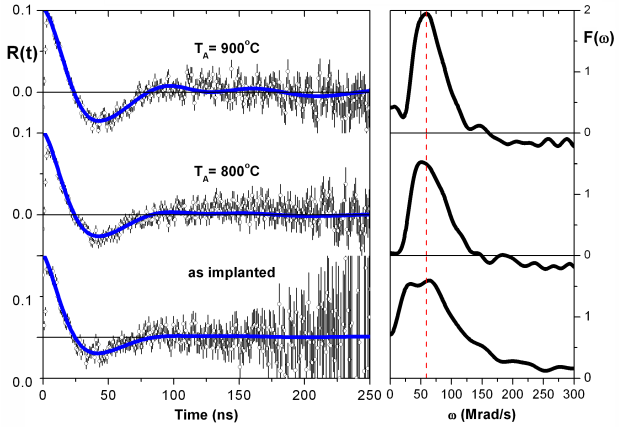

Figure 2 ^{111}Cd:$Cd_{0.16}Zn_{0.84}O$ γ-γ PAC from decay of ^{111m}Cd. Study as a function of annealing temperature under air. $T_M = RT$, Geometry: $M45$. **(left)** Counting rate ratio, $R(t)$. **(right)** Frequencies extracted from $R(t)$ after Fourier analysis.

parameters of the samples used in these works were not reported and quite an amount of different lattice parameters for bulk ZnO can be found [5,9,20]. Simulations were then performed with the parameters reported by H. Sowa and H. Ahsbahs [20], $a = 3.2489$ Å and $c = 5.2053$ Å, resulting in a $V_{zz} = 1.428 \times 10^{21}\,V/m^2$. In the same article, a study of those parameters as a function of pressure was done, so using the parameters found for a pressure of $6.92\,GPa$, $a = 3.2049$ Å and $c = 5.1216$ Å, resulted in a $V_{zz} = 1.672 \times 10^{21}\,V/m^2$. Hence, due to the fact that the V_{zz} is very sensitive to small variations of the lattice parameters and that V_{zz} increases, for Cd at the Zn site, with the decrease of the ratio c/a, the measured V_{zz}'s in ref.[22] and ref.[23] were probably done in samples with lattice parameters slightly different from the values used in the simulation.

The simulations confirm that the probes are incorporated on substitutional Zn-sites. Further DFT simulations considering different defect complexes are currently being performed in order to clarify the origin of EFG_2.

3.2 $Cd_{0.16}Zn_{0.84}O$ Figure 2 shows the PAC results obtained for $Cd_{0.16}Zn_{0.84}O$, which could be described by using a single fraction of probe nuclei interacting with a large static EFG distribution around a central value for all annealing temperatures. This indicates that, although the majority of the ^{111}Cd probes interact with a similar main EFG, implantation defects and intrinsic distortions due to

Table 2 ^{111}Cd:$Cd_{0.16}Zn_{0.84}O$ fitting parameters, related to Fig.2. ω_0 and $FWHM$ are given in $Mrad/s$ and V_{zz} is given in $10^{21}\ V/m^2$.

Annealing	ω_0	V_{zz}	η	$FWHM$
900^oC	37(1)	1.96(6)	0.5(1)	16.6(3)
800^oC				24.6(1)
600^oC				27.8(2)
400^oC				33.3(1)
As implanted				32.6(7)

crystal quality issues and the random distribution of Cd in the $Cd_{0.16}Zn_{0.84}O$ lattice are present, even after annealing at 900^oC. We point out that in such kind of ternary compounds both Cd and Zn atomic distributions do not follow a regular super-cell-like pattern. The Cd concentration is big enough to clearly change the mean lattice parameters, but at the same time it will contribute to the non-unique $EFGs$ that originate the large EFG distribution. The situation is clearly different from when implanting a small number of ^{111m}Cd atoms at the ppm concentration into the ZnO thin film. There, only implantation defects play a role and the Cd atoms themselves do not cause significant changes to the main ZnO EFG. Nevertheless, as can be seen by the fitting parameters in Table 2, the implantation defects contribution to the EFG distribution tend to be reduced as revealed by the decrease of the EFG distribution $FWHM$, with increasing annealing temperature. However, the attenuation of the curves remains high and little changes are observed in the PAC curves upon annealing.

The measurements indicate a higher central quadrupole frequency for the EFG distribution in $Cd_{0.16}Zn_{0.84}O$ compared to ZnO, which has the same crystalline structure (wurtzite), and the existence of a non-zero axial asymmetry parameter. A different magnitude of the quadrupole interaction frequency could be expected since the lattice parameters expand with increasing Cd content in the ternary film but the latter does not explain the observed asymmetry of the EFG. Since it is difficult to determine frequencies and asymmetry parameters on such attenuated spectra, two different sample orientation experiments have been performed regarding the PAC setup detectors, previously referred as the $M45$ and $M90$ measurement geometries. If a main orientation of a central EFG persists within the EFG distribution, different amplitudes for each of the three harmonic components that characterise the EFG should be observed in a consistent way. Therefore, the obtained results and correspondent Fourier transforms for ZnO and $Cd_{0.16}Zn_{0.84}O$ measured with the $M45$ setup and for $Cd_{0.16}Zn_{0.84}O$ measured with the $M90$ setup, all of them after annealing at 900^oC, are shown in Figure 3. By only changing the orientation angles, both fits of the $M45$ and $M90$ measurements give consistent results concerning quadrupole frequency and asymmetry parameter in the $Cd_{0.16}Zn_{0.84}O$, thus confirming that the central quadrupole frequency is higher than that obtained for ZnO. Still the observed non-zero axial asymmetry parameter reveals that from the local point of view of the ^{111m}Cd atoms the observed EFG does not reflect the expected axial lattice symmetry. This is most likely due to the incorporation of the implanted Cd ions in lattice environments, which were strongly distorted by the implantation defects and/or imperfections in the original lattice structure. These distortions around the probes are thermally very stable and annealing up to 900^oC provides only minor changes in the PAC curves. In order to get additional information on the macroscopic crystal quality, before and after implantation and annealing, RBS/C measurements were performed.

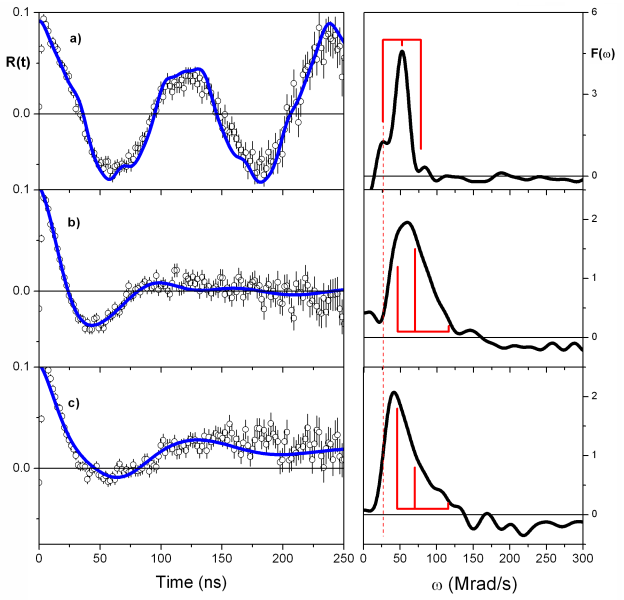

Figure 3 γ-γ PAC data of ZnO and $Cd_{0.16}Zn_{0.84}O$ annealed at 900^oC, from decay of ^{111m}Cd. **a)** ZnO, $M45$ setup. **b)** $Cd_{0.16}Zn_{0.84}O$, $M45$ setup. **c)** $Cd_{0.16}Zn_{0.84}O$, $M90$ setup.

Figure 4 shows RBS/C random and aligned spectra for the as-grown sample and after implantation and annealing at 400^oC and 900^oC. The as-grown sample shows a minimum yield of 10.9(2)% in the Cd-signal revealing a good crystal quality for a ternary compound. However the crystal quality is significantly worse than that expected for a perfect crystal, or even for the ZnO film which has a minimum yield of 2.7(1)% (not shown). After implantation and 400^oC annealing the minimum yield is slightly increased to 12.3(3)%. Annealing at 900^oC removes implantation damage and a minimum yield similar to the as-grown sample is recovered. However, the random spectrum shows that some Cd is lost during this thermal treatment. Nevertheless, it is worth mentioning that the MBE material studied shows a significantly better thermal stability than reported for $Cd_xZn_{1-x}O$ with similar composition grown by metal organic chemical vapour deposition which showed an almost complete loss of Cd for anneal-

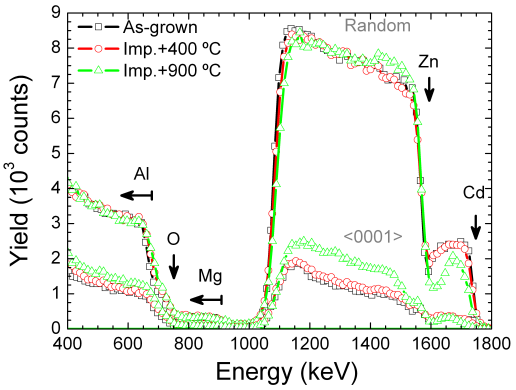

Figure 4 RBS/C random and $\langle 0001 \rangle$ aligned spectra of as-grown $Cd_{0.16}Zn_{0.84}O$ and after implantation and annealing at 400^oC and 900^oC.

ing at 900^oC [25]. In general, the RBS/C measurements show that the overall crystal symmetry and single crystalline character of $Cd_xZn_{1-x}O$ is preserved after implantation and annealing and no indications of phase separation due to the transformation of wurtzite to rocksalt phase are observed. PAC, on the other hand, reveals that very stable local distortions or defect complexes are formed in the implanted Cd probe's neighborhood and that thermal annealing does not improve this situation. The Cd-loss evidenced by RBS at the highest annealing temperature does not seem to influence the PAC results measured at the remaining $^{111m}Cd/^{111}Cd$ probe atoms, what further emphasizes the existence of highly stable defect complexes. Nonetheless, both RBS/C and PAC reveal the inefficiency of post-implant annealing treatments for $Cd_xZn_{1-x}O$ defect removal.

3.3 Ga_2O_3 The results for the pellet, Fig. 5a/Table 3, and for the nanowires, Fig. 5b/Table 4, are very similar, with two different fractions being observed, a EFG_1 frequency distribution characterized by a central frequency $\omega_{01} \approx 115\,Mrad/s$ (corresponding to $V_{zz1} = 6.08(5) \times 10^{21}\,V/m^2$), $\eta_1 = 0$ and almost nil $FWHM_1$, and a EFG_2 characterized by a bigger quadrupole frequency, $\omega_{02} \approx 140\,Mrad/s$ ($V_{zz2} = 7.40(5) \times 10^{21}\,V/m^2$), $\eta_2 = 0$, with a high static EFG distribution. In the Fourier transforms (right side of Figures 5a and 5b), ω_{01}, $2\omega_{01}$ and $3\omega_{01}$ are represented for EFG_1.

By comparing the V_{zz} obtained from DFT simulations (Table 5) to the experimental values, a perfect match is found for the first fraction (EFG_1) with the calculations assuming that the Cd probe is located in an octahedral Ga-site, where the experimental V_{zz} is only $\sim 1\%$ different from the simulation. However, the second fraction does not correspond to the substitutional tetrahedral site. The total energy of the crystal simulated for the Cd probe in the octahedral Ga-site was $0.47\,eV$ less than for the Cd probe in the tetrahedral Ga-site, hinting a preference of the probe for the octahedral site. Moreover, the distance to the nearest neighbours for the octahedral site is larger than for the tetrahedral site (Table 5), suggesting that the implanted ^{111m}Cd probes tend to occupy the Ga sites at the largest atomic position. The fact that, at the octahedral site, there are 6 oxygen first neighbours with distances between $2.115\,$Å and $2.218\,$Å, while at the tetrahedral site there are 4 oxygen neighbours with distances between $1.803\,$Å and $1.853\,$Å, allows an easier accommodation of the Cd ion in the first site. A further observation should be done to the fact that Ga^{3+} has an ionic radius of $0.62\,$Å while Cd^{2+} has an ionic radius of $0.95\,$Å, thus suggesting the preference of Cd incorporation in the octahedral site, where more space is available. As for the existence of the second fraction, revealing a highly attenuated EFG, it is probably due to remaining implantation defects, which could not be annealed. A previous study of Ga_2O_3 implanted with ^{111}In and also measured on ^{111}Cd was performed by A. F. Pasquevich *et al.* [26]. They report three different $EFGs$, two being similar to those observed by us. It has to be noted that PAC using the ^{111}In probe suffers from strong dynamic attenuation of the PAC spectra at RT due to so called "after effects" caused by the electron capture decay of the ^{111}In probe [26]. Therefore, Pasquevich *et al.* only see well defined PAC patterns for measurements at high temperatures ($> 500^oC$) where electron recombination is faster and after effects do not interfere. Like us, they attributed the $\omega_{01}\approx 113\,Mrad/s$ frequency to octahedral sites but they interpret the frequencies $\omega_{01}\approx 113\,Mrad/s$ and $\omega_{02}\approx 132\,Mrad/s$ as two different charge states (ionized and neutral, respectively) of the Cd acceptor. Since our measurements show those frequencies at room temperature where a negligible number of deep Cd acceptors should be ionized we tend to assign EFG_1 to the un-ionized Cd acceptor on the octahedral site and EFG_2 to sites influenced by residual implantation defects. Additional studies using higher annealing temperatures as well as a systematic study at different measuring temperatures is needed for a final assignment of EFG_2. Finally, Pasquevich *et al.* report a third EFG - absent in our measurement - with $\omega_{03}\approx 182\,Mrad/s$ which they assign to Cd on tetrahedral sites [26]. This assignment, however, is in disagreement with our simulation results predicting a smaller EFG for the tetrahedral site than for the octahedral site (see Table 5).

4 Conclusions and perspectives The usefulness of PAC in the study of nanostructures and thin films was demonstrated, allowing the observation of the local atomic environment around the probe and thus giving information about the lattice structure and probe's site. Two different case studies were analyzed, $ZnO/Cd_{0.16}Zn_{0.84}O$ thin films and a Ga_2O_3 powder pellet and Ga_2O_3 nanowires, all measured after implantation of $^{111m}Cd/^{111}Cd$ ($T_{1/2} = 48\,min.$). In the ZnO

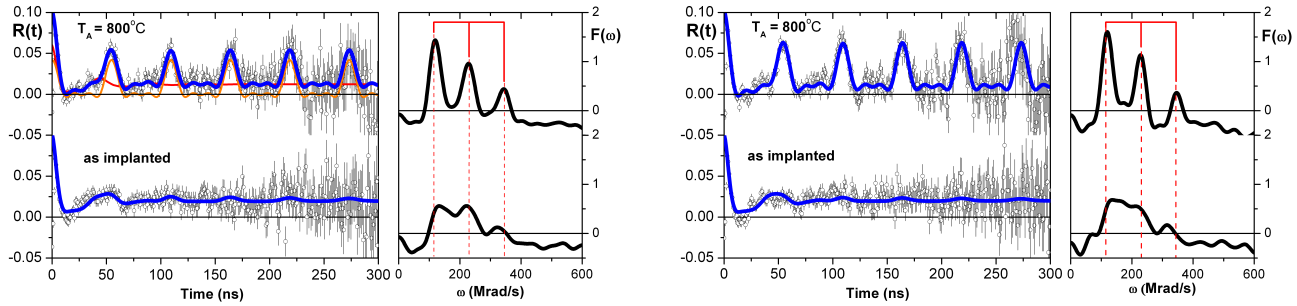

a) Powder pellet b) Nanowires

Figure 5 PAC curves and Fourier transforms for Ga_2O_3 pellets **(a)** and nanowires **(b)** for as-implanted samples and after annealing at 800^oC. $T_M = RT$, Geometry: $M45$. For $T_A = 800^oC$ in **(a)**, besides $R(t)$, fraction 1 is represented in orange and fraction 2 in red.

Table 3 ^{111}Cd:Ga_2O_3 powder pellet fitting parameters, related to Fig.5a. ω_0 and $FWHM$ are given in $Mrad/s$ and V_{zz} is given in $10^{21}\ V/m^2$.

Annealing	Fraction 1					Fraction 2				
	Perc.	ω_0	V_{zz}	η	$FWHM$	Perc.	ω_0	V_{zz}	η	$FWHM$
800^oC	41%	115(2)	6.08(6)	0.0(-)	0.0(-)	59%	140(3)	7.4(1)	0.0(-)	59.9(3)
As implanted	10%				6.9(7)	90%				79.0(9)

Table 4 ^{111}Cd:Ga_2O_3 nanowires fitting parameters, related to Fig.5b. ω_0 and $FWHM$ are given in $Mrad/s$ and V_{zz} is given in $10^{21}\ V/m^2$.

Annealing	Fraction 1					Fraction 2				
	Perc.	ω_0	V_{zz}	η	$FWHM$	Perc.	ω_0	V_{zz}	η	$FWHM$
800^oC	52%	115(1)	6.08(6)	0.0(-)	0.0(-)	48%	140(3)	7.4(1)	0.0(-)	55.5(6)
As implanted	9%				7.5(7)	91%				72.6(1)

Table 5 Simulated V_{zz} (V/m^2), for the Cd probe on a substitutional site of Ga in a $1 \times 2 \times 2$ supercell, for each non-equivalent Ga site in the unit cell, and distance to the nearest neighbours (Å)

Atomic site	$V_{zz}\ (sim.)$	Dist. nearest neighbours
Octahedral	6.02×10^{21}	2.115 - 2.218
Tetrahedral	4.67×10^{21}	1.803 - 1.853

case, two different fractions were observed, as have been previously found for bulk samples. The smaller EFG was attributed to Cd probes on undisturbed substitutional sites. A smaller quadrupole interaction frequency was obtained in the studied films compared to the results found on the literature for bulk samples, but XRD measurements showed different lattice parameters (a = 3.2405 Å, c = 5.2152 Å) than the values for bulk samples (a = 3.2489 Å, c = 5.2053 Å) [20], revealing a different strain state in the thin film and justifying this difference in the frequencies. DFT calculations performed with the measured lattice parameters showed excellent agreement with the experimental results and confirmed the high sensitivity to small changes in the lattice geometry of the EFG probed by the radioactive Cd atoms incorporated at Zn-sites in the thin films. The larger EFG only appeared after annealing and was attributed to the trapping of a defect, possibly an oxygen vacancy, in the vicinity of the probe. The ternary alloy $Cd_{0.16}Zn_{0.84}O$, although having a wurtzite structure similar to ZnO, showed higher quadrupole frequencies, possibly due to the expansion of the lattice parameters with the Cd content, as well as a non-zero asymmetry parameter and large static distributions in the EFG, which were attributed to the clustering of defects close to the probe, even after annealing. The nontrivial differences observed at the nanoscopic scale between high-quality epitaxial thin films of ZnO, where ^{111m}Cd appears as a highly diluted probe, and on $Cd_xZn_{1-x}O$ alloy where the Cd is at the % range, encourage a systematic study for different Cd concentrations, from highly diluted to the % range, in fine increasing steps, aiming the observation and identification of defects forming and segregating with increasing x. In the Ga_2O_3 case, both the powder pellet and the nanowires showed the existence of two different fractions, where the first one is attributed to Cd probes in the substitutional octahedral Ga-site and the second one is not understood, but probably results from the existence of residual implantation defects that could not be annealed. Nonetheless, the

similarity between the results for the powder pellet and the nanowires demonstrates that efficient doping of nanowires by ion implantation is conceivable.

Acknowledgements This work was performed within the ISOLDE proposal IS481 and supported by FCT-Portugal, project CERN-FP-123585-2011 and by the European Union FP7-through ENSAR, contract 262010. We acknowledge a scholarship from project FCT CERN-FP-116320-2010 and support by grants PTDC/CTM/100756/2008, PTDC/CTM-NAN/2156/2012, Ciência 2007, SFRH/BPD/74095/2010 and SFRH/BPD/82059/2011 (FCT, Portugal). The authors further acknowledge the ISOLDE collaboration for supportive access to beam time.

References

[1] C. M. Lieber and Z. L. Wang, MRS Bulletin **32**(02), 99–108 (2007).
[2] S. Kalusniak, S. Sadofev, J. Puls, and F. Henneberger, Laser & Photonics Reviews **3**(3), 233–242 (2009).
[3] E. Nogales, P. Hidalgo, K. Lorenz, B. Méndez, J. Piqueras, and E. Alves, Nanotechnology **22**, 285706 (2011).
[4] G. Schatz and A. Weidinger, Nuclear Condensed Matter Physics: Nuclear Methods and Applications (Wiley, New York, 1996).
[5] U. Özgür, Y. I. Alivov, C. Liu, A. Teke, M. A. Reshchikov, S. Dogan, V. Avrutin, S. J. Cho, and H. Morkoc, Journal of Applied Physics **98**(4), 041301 (2005).
[6] R. Dogra, A. Byrne, and M. Ridgway, Optical Materials **31**(10), 1443 – 1447 (2009), Including Special Issue: Papers from the Fourth Workshop on Cryogenic Scintillation CryoScint08.
[7] V. Venkatachalapathy, A. Galeckas, M. Trunk, T. Zhang, A. Azarov, and A. Y. Kuznetsov, Phys. Rev. B **83**(Mar), 125315 (2011).
[8] X. F. Fan, H. D. Sun, Z. X. Shen, J. L. Kuo, and Y. M. Lu, Journal of Physics: Condensed Matter **20**(23), 235221 (2008).
[9] P. Kessler, K. Lorenz, and R. Vianden, Defect and Diffusion Forum **311**, 167–179 (2011).
[10] S. Geller, The Journal of Chemical Physics **33**(3), 676–684 (1960).
[11] H. H. Tippins, Phys. Rev. **140**(Oct), A316–A319 (1965).
[12] C. H. Liang, G. W. Meng, G. Z. Wang, Y. W. Wang, L. D. Zhang, and S. Y. Zhang, Applied Physics Letters **78**(21), 3202–3204 (2001).
[13] I. Lopez, E. Nogales, B. Mendez, and J. Piqueras, Applied Physics Letters **100**(26), 261910 (2012).
[14] A. Redondo-Cubero, M. Brandt, F. Henneberger, E. Alves, and K. Lorenz, Proc. of SPIE **8263**, 82630U (2012).
[15] J. Blachot, Nuclear Data Sheets **110**(6), 1239 – 1407 (2009).
[16] N. Stone, Atomic Data and Nuclear Data Tables **90**(1), 75 – 176 (2005).
[17] T. Butz, S. Saibene, T. Fraenzke, and M. Weber, Nuclear Instruments and Methods in Physics Research Section A: Accelerators, Spectrometers, Detectors and Associated Equipment **284**, 417 – 421 (1989).
[18] E. Nogales, B. Méndez, J. Piqueras, and J. A. García, Nanotechnology **20**, 115201 (2009).
[19] F. Litimein, D. Rached, R. Khenata, and H. Baltache, Journal of Alloys and Compounds **488**(1), 148 – 156 (2009).
[20] H. Sowa and H. Ahsbahs, Journal of Applied Crystallography **39**(2), 169–175 (2006).
[21] P. Blaha, K.S., G. Madsen, D. Kvasnicka, and J. Luitz, Techn. Universität Wien (2001).
[22] M. E. Mercurio, A. W. Carbonari, M. R. Cordeiro, R. N. Saxena, and L. Z. D'Agostino, Journal of Magnetism and Magnetic Materials **322**(May), 1195–1197 (2010).
[23] H. Wolf, S. Deubler, D. Forkel, H. Foettinger, M. Iwatschenko-Borho, F. Meyer, M. Renn, W. Witthuhn, and R. Helbig, Materials Science Forum **10-12**, 863–868 (1986).
[24] P. Kessler, Implantationsschäden in polaren und unpolaren ZnO Einkristallen, Master's thesis, Helmholtz-Institut für Strahlen- und Kernphysik, Universität Bonn, 2008.
[25] A. Y. Azarov, T. C. Zhang, B. G. Svensson, and A. Y. Kuznetsov, Applied Physics Letters **99**(11), 111903 (2011).
[26] A. F. Pasquevich, M. Uhrmacher, L. Ziegeler, and K. P. Lieb, Phys. Rev. B **48**(Oct), 10052–10062 (1993).